KSME Journal, Vol. 8, No. 2, pp. 161~174, 1994

Aerodynamic Noise Generation in Centrifugal Turbomachinery

Jong-Soo Choi*

(*Received July 23, 1993*)

The objective of this research was to identify which aspects of the fluid dynamics are associated with noise generation in centrifugal turbomachinery. Research emphasis was placed on the generation of noise at frequencies other than the blade passage tones. In order to avoid noise generated by the interaction of the discharged flow and stationary objects outside of the impeller, experiments are performed on a centrifugal impeller without diffuser and casing. With this discharge configuration, the radiated noise spectra are shown to be dominated by harmonically related broad humps at low frequency. These were proven to be generated by the interaction of a coherent unsteady flow structure rotating around the impeller discharge and the trailing edges of the impeller blades.

Key Words: Centrifugal Impeller, Centrifugal Turbomachinery, Aerodynamic Noise, Discharge Flow Instability, Trailing Edge Noise

Nomenclature

a : Speed of sound
b : Impeller blade width
C : Length of the impeller blade along the surface
D : Impeller diameter
f : Frequency (Hz)
F : Acoustic source spectral distribuition function
G : Acoustic frequency response function
L : Non-dimensional power spectral density
m : Azimuthal mode number
p : Pressure
p_{ref} : Reference acoustic pressure (20 μPa)
Q : Volume flow rate
r : Radius in cylindrical coordinates
R : Impeller radius
U : Phase averaged mean velocity in rotating coordinates
V : Phase averaged mean velocity in laboratory coordinates
V_{tip} : Impeller tip speed ($R\Omega$)
z : Axial distance from the shroud
Z : Number of impeller blades (7)
r : Radial distance from the impeller
He : Helmholtz number (fD/a)
St : Strouhal number based on the impeller tip speed ($\pi D/Z)(f/V_{tip}$)
ρ_o : Standard air density (1.21 kg/m^3)
ϕ : Flow coefficient ($Q/\pi bDV_{tip}$)
ψ : Head rise coefficient ($\Delta p/V_{tip}^2$)
ω : Angular rotational speed of the instability pattern (rad/sec)
Ω : Angular rotational speed of the impeller (rad/sec)

Subscripts

p : Pressure
r : Radial
R : Rotating coordinates
S : Stationary coordinates
u : Velocity in rotating coordinates
v : Velocity in stationary coordinates

* The Pennsylvania State University, Currently in Chungnam National University, Korea

1. Introduction

In centrifugal turbomachinery, the noise generated is often dominated by tones at the blade passage frequency and higher harmonics. This is a consequence of the strong interaction between the

periodic flow discharged radially from the impeller and the stator blades or cutoff leading to the exit duct. A spatially distorted inlet flowfield interacting with the rotor may also generate similar tones. In addition to these, broadband noise may be generated by trailing edge/flow interaction, turbulent boundary layers and separated flow on the impeller blade and housing. Past research has focussed mainly on the generation and reduction of the blade passage frequency tones. This has led to the noise generation mechanism of these tones being relatively well known. Several techniques have been successful in controlling this type of noise. Little work has been done, however, on identifying or reducing the broadband noise sources.

In centrifugal turbomachinery both types of noise generation mechanisms can occur simultaneously. Tourret et al.(1985) have tested a centrifugal pump with a casing and found that the most severe pressure fluctuations occur at the volute cut-off. This type of noise generation mechanism is well defined. The efforts aimed at reducing the levels of this interaction noise by changing the impeller and cut-off geometry is summarized in the literature survey by Neise(1976). Embleton(1963) has implemented several design changes in the impeller and cut-off, such as sloping the cut-off and impeller blades and slots in impeller blades. The approach was, however, based on intuition and a parametric study.

Compared to interaction noise, the sources of broadband noise in turbomachinery are not well understood. Broadband noise is generated by the flow through the impeller and casing. It is anticipated, however, that the most severe broadband noise sources are associated with the turbulent flow in the impeller passages and the unsteady discharge flow. In order to understand the broadband noise generation mechanisms, therefore, precise knowledge on the flow behavior in the impeller is very important. The objective of this study is to develop a fundamental understanding of the unsteady flowfield which generates broadband noise in centrifugal turbomachinery, in particular centrifugal pumps. Emphasis is placed on the noise sources associated with the impeller. The unique approach adopted in this research is to determine noise sources by careful measurement of the fluid dynamics and acoustics.

2. Experimental Approach

2.1 Test facility

In this research, aerodynamic and acoustic measurements are performed on a centrifugal water pump using air as the fluid medium. Switching fluid media for testing is not unusual in the pump or compressor industry (Gilman, 1968). This is often done when the design fluid used is expensive or difficult to handle. For example testing a rocket engine turbo pump in air has been examined by King(1968). It was found that a very good correlation exists between the air and liquid test data. Based on this reasoning, the advantages in performing experiments using air instead of water, such as easier instrumentation, operation and simpler test setup, are worthwhile. Further details on the influence of different fluid media on the aerodynamic and the acoustic characteristics were summarized in Choi(1991).

As stated before, it is anticipated that the broadband noise sources in centrifugal machines are aerodynamically interrelated. It is, therefore, difficult if not impossible to isolate and study each noise source by measuring the radiated noise alone. To overcome this difficulty, the isolation of the phenomena of interest was accomplished by experiments performed on a centrifugal pump in a simplified configuration. For the purpose of these experiments, the impeller is allowed to discharge to the atmosphere so that any interaction noise generated by the discharged flow and stationary objects outside of the impeller is removed. In addition to developing a fundamental understanding of the noise sources, the study has direct application to the class of centrifugal turbomachines that collect the discharged fluid without a cut-off or diffuser stator vanes. The effect of discharge configuration on both the flow and the generated noise is being examined in a continuing study by Bent(1993).

As shown in Fig. 1, a commercial water pump

impeller (Worthington Model D-1011) was chosen for the experiment. The impeller has seven backward swept blades with a discharge angle of about 21 degrees to the tangent. The impeller has a curved front shroud while the hub is relatively flat and perpendicular to the inlet flow direction. The inlet and discharge diameters of the impeller are 133.4 mm and 320.0 mm, respectively. The experimental facility (shown in Fig. 2) is designed for the quiet operation of a centrifugal turbomachine without an outer casing. A specially designed (quiet) drive system is used to power the impeller at any rotational speed up to 3600 rpm. The rotational speed of the impeller is measured with an optical shaft encoder placed between the motor and the bearings. The inlet flow is controlled by an upstream flow management unit, including a bellmouth inlet, turbulence management screens, honeycomb and a duct. Part of the upstream ducting is also an anechoic termination

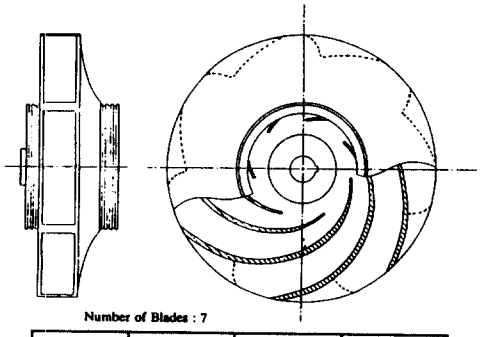

	Diameter	Blade Angle	Blade Width
Inlet	133.4 mm	11 deg.	57 mm
Discharge	320.0 mm	21 deg.	40 mm

Fig. 1 Tested centrifugal Impeller

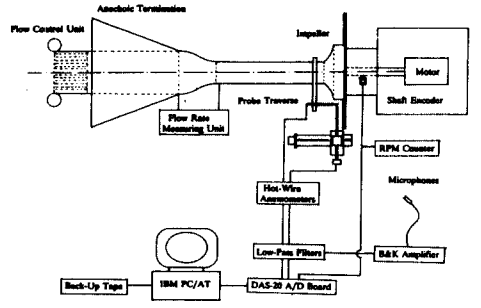

Fig. 2 Test setup and data acquisition system

that is used to minimize standing waves in the duct. All experiments are conducted in the anechoic chamber of the Center for Acoustics and Vibration at Penn State University. Noise propagating up the inlet duct is measured with two flush mounted B&K condenser microphones (Model 4181). Further details on the experimental facility and noise measurement techniques are reported in Choi(1991) and Mongeau(1991). A digital data acquisition and analysis system based on an IBM PC/AT compatible computer and a Metrabyte DAS-20 12 bit A/D converter is used to acquire and analyze data. To avoid aliasing problems in digital signal processing, low pass analog filters (Ithaco Model 4302) are used in all measurements.

2.2 Flow parameters

The impeller performance characteristics are determined by the static pressure difference between the impeller inlet and the discharge at various flow rates. The non-dimensional static pressure rise through the impeller ($\psi = \Delta p / V_{tip}^2$), plotted versus flow coefficient ($\phi = Q/\pi bDV_{tip}$) constitutes the non-dimensional operating curve for the impeller. When the characteristic curves are plotted in non-dimensional form (ψ vs. ϕ), the two curves measured at the shaft speed of 2400 and 3000 rpm's collapse well. This suggests that the non-dimensional parameters have been properly chosen. From manufacturer's data it was determined that the impeller was originally designed to have maximum efficiency at $\phi = 0.062$. Extensive flow and noise measurements were performed over a wide range of flow rates, and showed a most predominant flow instability at $\phi = 0.09$. This discharge flow instability is found to be a major aerodynamic noise source in the centrifugal impeller when it is operated without a casing or diffuser blades. In this investigation, therefore, most of experimental results are presented at three representative operating conditions; high ($\phi = 0.12$), medium ($\phi = 0.09$) and low flow rate ($\phi = 0.06$).

2.3 Experimental procedure

Hot-wire sensors are ideal for the measurement of turbomachinery flows because of their high frequency response, low noise level, and fine

spatial resolution. At the discharge of the impeller, the unsteady discharge flowfield was measured with a crossed hot-wire probe (TSI Model 1241-T1.5). The crossed-wire probe calibration procedure and data processing techniques used in these experiments followed those of Westphal and Mehta(1984). The measuring accuracy of the velocity magnitude and yaw angle are $\pm 2\%$ and ± 2 deg., respectively, for yaw angles up to ± 35 degrees.

In addition to the discharge flow measurement, the velocity in the rotating frame is measured with a hot-wire mounted on the impeller. The small size and the light weight of the probe made it possible to operate the impeller with the probe attached at speeds up to 2400 rpm without unbalancing the impeller. The lead wires from the hot-wire probe were connected to a slip-ring unit mounted on the impeller shaft. The slip-ring unit used in this experiment, Model IECFCS-2-10 by IEC Corporation, has 10 channels and each channel has four silver graphite contacts for signal transmission. The hot-wire anemometer bridge was balanced and calibrated with and without the slip-ring unit and showed identical calibration characteristics in both cases.

It has been shown by Hah & Lakshminarayana(1978) that the effect of centrifugal forces of the rotating hot-wire on the calibration is negligible. In their experiment the rotation of the probe was varied from 800 to 1200 rpm which corresponded to a centrifugal acceleration of 500 to 700 g. Only a 1.5 % increase in cold resistance was found for the range of the experiments. The change in cold resistance was presumably due to the elongation of the wire by centrifugal force. In the present experiments, the centrifugal acceleration was 500 g for the rotational speed of 1680 rpm and the probe mounted at the trailing edge of the impeller. It is proven that data taken at higher rotational speed (up to 2400 rpm) collapse very well with lower rpm's when scaled properly. Therefore, in the present experiments, no adverse effects of the hot-wire rotation on its output is expected.

To measure the unsteady static pressure on impeller blades, pressure transducers manufactured by the PCB corporation (model 103A11) were selected. The sensor has a cylindrical shape, 9.4 mm in diameter and 5.6 mm in height, and weighs 2.3 grams. Pressure is sensed through a 2.5 mm diameter orifice on one side of the sensor. Only the unsteady component of pressure is sensed, because of the characteristics of the piezoceramic materials used in the sensor. The sensor has a built-in amplifier and vibration compensating accelerometer which produces a high signal-to-noise ratio. The small size, high sensitivity and high frequency response of the sensor have proven to be adequate for this application.

As illustrated in Fig. 3, the impeller blade surface pressure is measured by a sensor attached to the opposite side of an impeller blade through a 2.5 mm diameter pin-hole. The resonance frequency of the cavity inside the pin-hole was estimated to be 20 kHz. The pin-hole was covered with aluminum tape to determine the noise level of the sensor signal due only to mechanical and electrical sources during impeller operation. Inoverall comparison the signal-to-noise ratio is more than 15 dB for the frequency range of interest (between 100 Hz and 800 Hz).

The power spectral densities measured from hot-wires and pressure transducers are normalized with the following parameters: The square of the impeller tip speed is used for the power spectral density of velocity G_{uu}. A dynamic pressure based on V_{tip} is used for the power spectral density of the pressure G_{pp}. The resulting non-dimensional power spectral densities are:

$$L_{uu}(St) = 10 \log[G_{uu}(f)/V_{tip}^2(\frac{D}{V_{tip}})] \qquad (1)$$

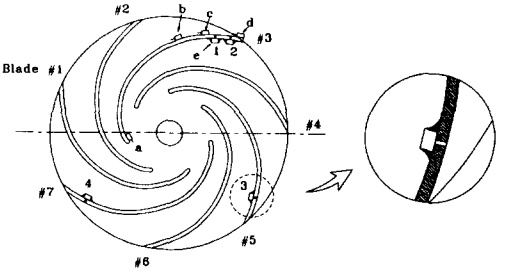

Fig. 3 Rotating hot-wire and pressure sensor locations

$$L_{pp}(St)=10\log[G_{uu}(f)/\rho_o^2 V_{tip}^4(\frac{D}{V_{tip}})] \quad (2)$$

For the spectra presented in this paper, the number of data was 1024 and the sampling frequency was 2 kHz for each channel, so the frequency bin width (Δf) was 1.95 Hz. One hundred averages were performed with a 50% overlap and a Hanning window was used to taper each 1 kByte long record.

3. Experimental Results

3.1 Radiated noise from a centrifugal impeller

Noise was measured with microphones both in the inlet duct and in the acoustic far-field of the impeller. A technique using acoustic similarity laws was applied to separate the acoustic source strength from the effects of noise propagation. The cross-spectra shown in Fig. 4 are from two microphones diametrically flush mounted in the inlet duct. The abscissa has units of frequency (Hz) along with Helmholtz number (He), the non-dimensional frequency scaled by speed of sound (a) and the impeller diameter (D):

$$He=\frac{fD}{a} \quad (3)$$

The purpose of using the cross-spectrum technique is to eliminate flow turbulence noise from the microphone signal. The spectra shown in Fig. 4 were measured at various rotational speeds, keeping the non-dimensional flow rate constant. With higher shaft speed, some peaks increased in frequency. Most of the strongest peaks in the spectra, however, stayed at the same frequency. In other words, there are some characteristics of the noise spectra that are shaft speed dependent and some that are independent. The shaft speed dependent characteristics can be more easily identified by scaling the frequency on the abscissa with shaft speed. In non-dimensional form this is known as the Strouhal number (St),

$$St=\frac{\pi D}{Z}\frac{f}{V_{tip}}=\frac{f}{BPF} \quad (4)$$

The data in Fig. 5 are the same as that in Fig. 4 except the abscissa is non-dimensionalyzed (St), instead of in Hertz. The peaks at $St \approx 1.3$ of each curve align very well. Later it will be proven that these peaks are related to a fluid dynamic phenomena.

To summarize, two different factors contribute to the spectral distribution of the radiated noise. Helmholz effects are related to acoustical phenomena such as radiation efficiency, resonances or directivity patterns. Strouhal effects are related to the fluid mechanics, and therefore to the aerodynamic noise generation process. These two aspects can be spectrally decomposed and the interpretation of the acoustic measurements can be greatly facilitated. A technique developed to separate these two spectral trends is discussed in the following section.

The technique used by Mongeau(1991) followed the spectral decomposition approach developed by Neise and Barsikow(1982) based on a simple product law model. The technique separates the measured noise spectra (S_{pp}) into a source strength spectral distribution function (F

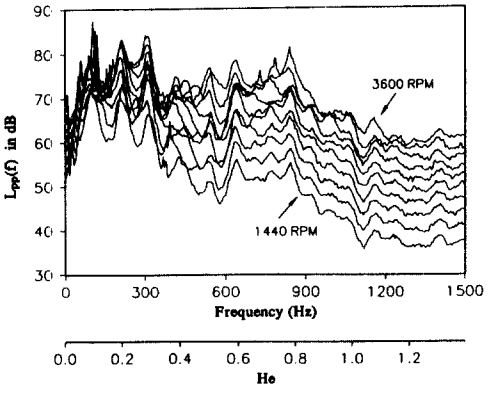

Fig. 4 Sound pressure level vs. frequency

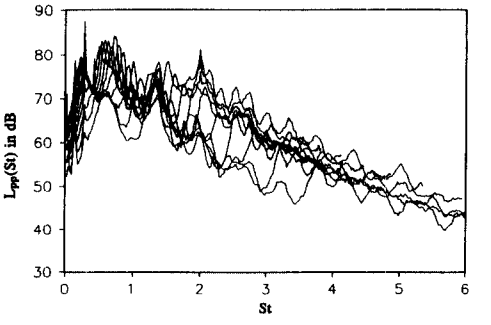

Fig. 5 Sound pressure level vs. Strouhal number

function) and an acoustic frequency response function (G function). In mathematical form,

$$\frac{\sqrt{S_{pp}(f)}}{\rho_o V_{tip}^2 \sqrt{\frac{D}{V_{tip}}}} = G(He, \phi) \cdot F(St, \phi) \quad (5)$$

By taking 20 times the logarithm of both sides of the equation, the sound spectral level (L_{pp}) becomes a summation of the logarithm of the G and F functions along with some scaling constants ; that is :

$$\begin{aligned} L_{pp} &= 10\log[\frac{S_{pp}\Delta f}{P_{ref}^2}] \\ &= 20\log G(He) + 20\log F(St) \\ &\quad + 30\log V_{tip} + 90.7 \end{aligned} \quad (6)$$

For a fixed Strouhal number, the F function is a constant, so it is possible to calculate the G function from the measured sound spectral densities at different shaft speeds. Further details on this procedure can be found in Mongeau(1991).

The numerous source strength spectral functions (F functions) presented in Fig. 6 are processed from the measured noise spectra at 10 different rpm values shown in Fig. 4. The flow rate coefficient was fixed at $\phi=0.09$ for each case. All the spectra collapse, within a few dB, into a single curve. This is a strong indication of the validity of the model. The spectra obtained are more representative of the noise source spectra which were buried in the other acoustic characteristics such as duct resonance or directivity effects. This technique resulted in a much easier interpretation of the spectra of the noise source. It has also allowed a direct tie to be established between the acoustics and the aerodynamics. The dimensional analysis involved also provides critical information as to the proper scaling of the acoustic data for changes in the fluid medium and impeller geometry.

The unusual feature of the spectra of Fig. 6 is the large component of radiated noise at $St \approx 0.7$, 1.4, 2.1, etc, instead of the predominant noise occurring at the blade passage frequency ($St=1.0$) and its harmonics. The F functions for the flow rates $\phi=0.06$ and $\phi=0.12$ are also performed and showed similar trend. The frequency and the level of the peaks depends on the flow rate. There is a regular increase in frequency with flow rate, and an almost perfect harmonic relationship is maintained between the center frequency of each of the humps. The level of the first three humps is highest at $\phi=0.09$, i.e., 15 to 25 dB above the random part of the spectrum. Since this was the case, the aerodynamic measurements designed to identify the aerodynamic noise generation mechanism were focused at this flow condition. The objective of the present research focuses on the identification of the spectral humps shown in Fig. 6.

3.2 Flow measurement at the discharge

The hot-wire data measured at the impeller discharge have strong periodicity at the impeller blade rate. This was determined from the measured signal by using a synchronous averaging technique. Hot-wire data were sampled in conjunction with a signal from a shaft encoder which generated a 5 volt pulse once per revolution of the impeller. This signal is used as a reference to average the hot-wire data for one hundred impeller revolutions.

Figure 7 shows the measured discharge velocity

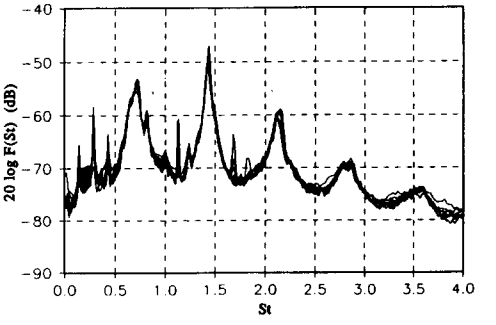

Fig. 6 Source spectral density function

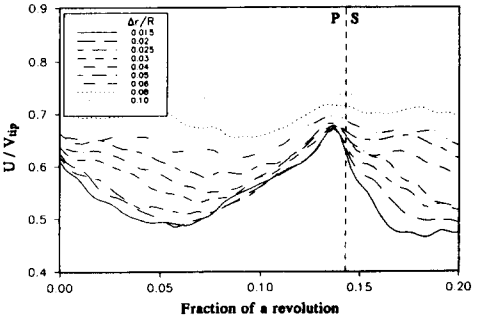

Fig. 7 Measured discharge velocity amplitudes in rotating coordinates

magnitude in the rotating (impeller) coordinate frame at various radial positions. The probe was placed at mid-passage, i.e., $z/b=0.5$, and the impeller was operated at the flow rate $\phi=0.09$. The impeller tip speed was used to non-dimensionalize these quantities. The horizontal scale, marked fraction of a revolution, begins at the trailing edge of impeller blade #1. The locations of the second blade trailing edge is marked with a vertical dotted line. The pressure and suction sides of each blade are marked with P and S on opposite side of the dotted lines, respectively. The pressure side corresponds to the convex side of a blade, because the blades are swept backward.

The discharge velocity pattern (in rotating coordinates), shown in Fig. 7, clearly show a high velocity (jet) region near the pressure side of a blade compared to the low velocity (wake) region in the suction side. This jet and wake type of flow pattern has been observed by many other investigators in centrifugal turbomachinery experiments (Dean & Senoo, 1960; Fowler, 1968; Eckardt, 1975). At all three flow rates, the discharge flowfield shows a shear region on either side of the jet. Especially, a high shear region is found near the trailing edge of each blade where mixing between the jet and wake occurs. This flow mixing is so rapid that the jet-wake pattern cannot be identified even before the flow reaches a distance of 10% of the radius from the impeller.

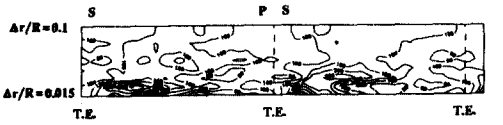

Fig. 8 Axial vorticity distribution

This flowfield can be separated into a spatially uniform flow and a vortical flow motion. The average vorticity strength whose axis is parallel to the trailing edge of blades can be quantified by using the phase averaged velocity components in relative coordinates. Figure 8 shows contours of axial vorticity at the mid-passage ($z/b=0.5$) of the impeller discharge for $\phi=0.09$. The figure is generated from the radial and tangential components of velocities measured at 10 radial locations between $\Delta r/R=0.015$ and $\Delta r/R=0.1$. The scale of the y-axis in the figure is expanded by 5 times to clarify the vorticity distribution.

The strong vorticity field found near the blade trailing edge indicates a possible flow movement from one passage to another in the form of a roll-up around the blade trailing edge. This is strongly indicated by the small discharge flow angle and the small radial velocity near the suction side of the blade. The proposed flow behavior is observed from the time trace of the instanta-

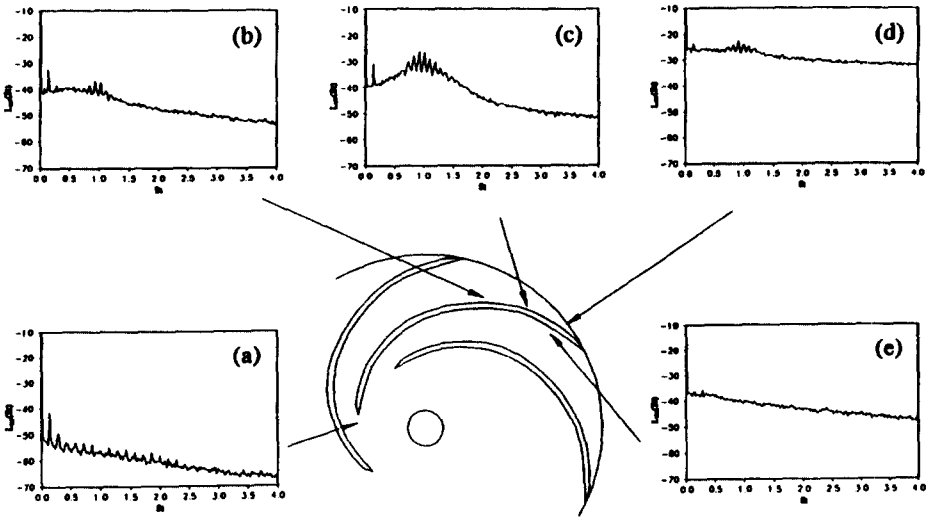

Fig. 9 Velocity spectra measured with a rotating hot-wire at $\phi=0.06$

neous radial velocity. A negative radial velocity is found intermittently near the suction side and is apparent in all three flow rate cases. This unsteady backflow is believed to disturb the passage flow, and consequently induces the unsteady pressure fluctuation on the blade surface.

3.3 Unsteady flow in an impeller passage

In an attempt to establish how the unstable flow is generated and distributed, a series of hot-wire and unsteady pressure measurements were made in the vane passages. Figures 9, 10 and 11 show the measured spectra with a rotating hot-wire at various locations above a blade surface for flow rates $\phi=0.06$, $\phi=0.09$ and $\phi=0.12$, respectively. The detailed sensor locations are shown in Fig. 3. For all three cases, a cluster of spectral peaks appeared near the trailing edge on the pressure side of the blade. The inlet flow spectra measured with a hot-wire sensor at "a" showed low amplitude, or low turbulence level, for all flow rates. The only tones found in the spectra are related to the shaft rate and its har-

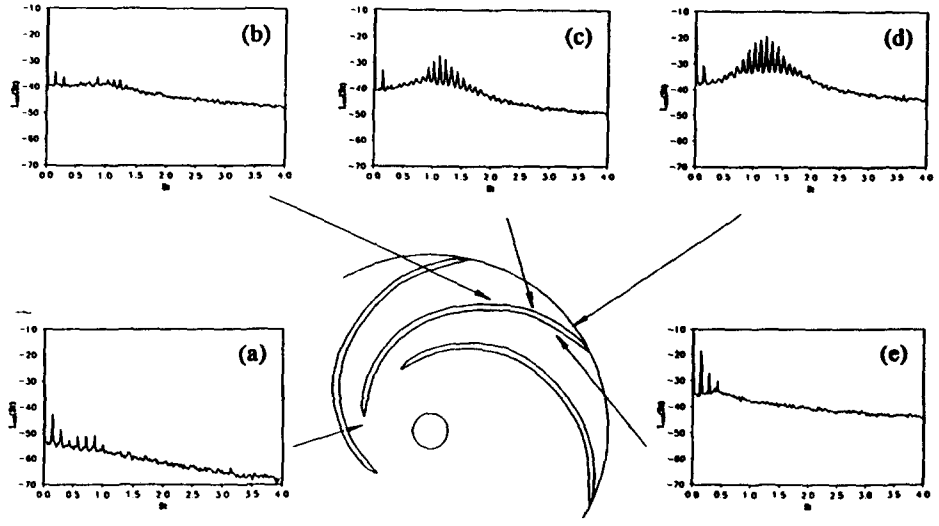

Fig. 10 Velocity spectra measured with a rotating hot-wire at $\phi=0.09$

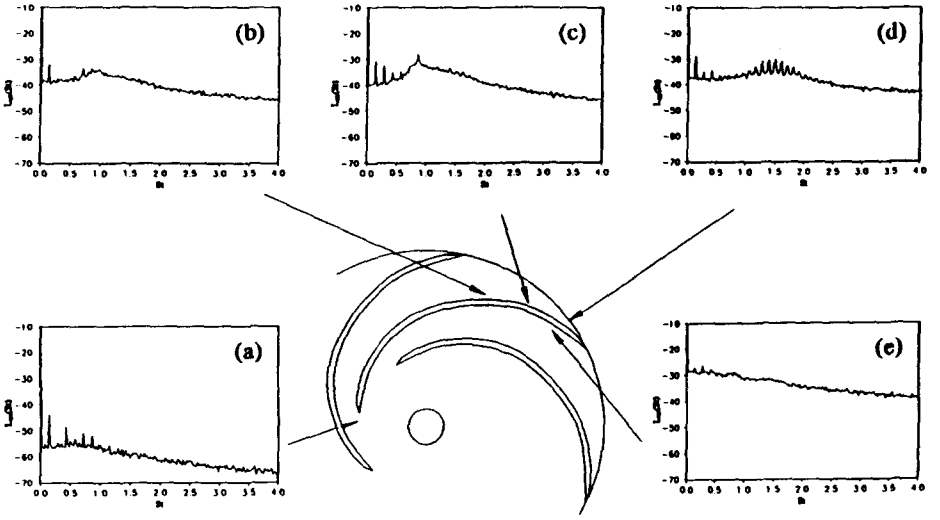

Fig. 11 Velocity spectra measured with a rotating hot-wire at $\phi=0.12$

monics, which are presumably due to the noise from the slip-ring unit and from slight asymmetries in the impeller geometry. The random level of the spectra increased progressively from sensor location "a" to "b" to "c". It is believed that the thickening boundary layer on the pressure side of a blade surface influences the turbulence level as the flow moves downstream.

At flow rates $\phi=0.06$ and $\phi=0.09$, the cluster of peaks is first observed at position "b" and become stronger closer to the trailing edge. At location "d" of Fig. 9, however, the peaks are buried under a high random spectrum level. By comparing spectra at "b" for the three flow rates, the cluster of peaks are more identifiable at $\phi=0.06$ than the other two, suggesting that the flow disturbances that generate the peaks started earlier in this case. The sensor "b" is located approximately where an impeller channel formed by two adjacent blades ends. So, the rest of the blade, starting from the position "b", is directly exposed to the impeller discharge region. The flow leaving this passage is being influenced by the external flow and experiencing sudden pressure changes. The reason why the disturbance started earlier in the upstream passage at $\phi=0.06$ is probably due to the lower radial velocity level compared to the other flow rates, so it is strongly suspected that the disturbances have less radial flow momentum to work against at the discharge. The disturbances at the discharge destabilize the passage flow, and consequently induce pressure fluctuation on the blade surface.

In Fig. 12, the surface pressure spectrum measured with pressure transducer "2" whose pinhole is located just below the rotating hot-wire sensor "d" is presented. The gap between the hot-wire and the blade surface was about 5 mm. The similarity in spectral shape of figures 12 and 10(d) indicates a strong correlation between the unsteady velocity and the pressure near the surface. In particular, the spectral peaks between Strouhal numbers of 0.5 and 2.0 suggest that a well organized aerodynamic motion exists that causes a periodic pressure fluctuation on the surface. Each peak in this cluster is separated by a uniform spacing of $St\approx0.1$. The cluster is centered about $St\approx1.2$. In order to distinguish between individual peaks, an integer number is assigned to each of them, obtained by dividing the Strouhal number of each peak with the peak spacing. In other words, the peak at $St\approx0.7$ is named $m=7$ and the one at $St\approx0.8$ is $m=8$, etc. This organized flow motion in one passage is found to be related to the unsteady flow in the other passages. The disturbance from a passage propagates over the flow discharged from adjacent passages and creates a coherent flowfield around the impeller. In the following section more about this organized flow phenomena is discussed.

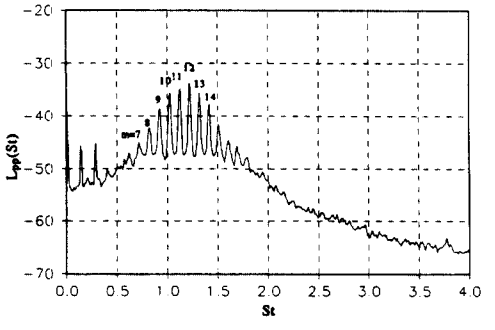

Fig. 12 Power spectral density of surface pressure at 2

3.4 Surface pressure correlation between blades

The influence of a passage flow on the adjacent passages can be examined from the cross-correlation between pressure transducers mounted on different blades. Three pressure sensors, labeled with 1, 3 and 4, were mounted on blades 3, 5 and 7 respectively (Fig. 3). The radial and axial location of these sensors was identical relative to each blade. Shown in Fig. 13(a) and 13(b) are the coherence and phase angle between sensor 1 and 3, respectively. As shown in Fig. 13(a), the coherence level of those corresponding peaks found in Fig. 12 is more than 0.8. This indicates that the flow disturbances which generate the spectral peaks in the spectra are highly correlated between blades even though these blades are separated by two blade passages. Similar phenomena is also observed from the coherence between blade 3 and 7 separated three passages apart. The

negative peaks in the coherence spectra, however, dropped even further compare to the ones in Fig. 13(a), while the amplitude of the positive peaks remained at almost the same level. Compared to the peaks with integer mode numbers, the negative peaks between $St=0.7$ and $St=2.5$ correspond to the non-integer mode numbers. The unsteady flow motion that generates such non-integer modes is not coherent between blades. It is appropriate here to mention the reason why the measured spectra show only modal peaks with integer number. When an arbitrary wave pattern is formed around a circle, the pattern has a periodicity of 2π. The Fourier transform of this pattern, therefore, has Fourier components only with periodicity at multiples of 2π. If the pattern is distorted by random signals which are not correlated around the circle, the pattern loses some of its periodicity.

The unsteady flow that is coherent from blade to blade forms a rotating pattern, and the pattern precesses around the impeller. The precessing speed can be estimated from the phase relation between signals from two pressure transducers on different blades. Shown in Fig. 13(b) is the phase angle of the cross-spectra between sensor 1 and 3. The linear phase relation between $St=0.5$ and $St=2.5$ indicates that each mode rotates around the impeller with an almost equal speed. The time delay is estimated from the phase angle and then used with the sensor separation distance measured along the circumference to estimate the wave length of a signal. The rotational speed (ω_R) of the pattern at $St=0.72$ is calculated to be 72% of the shaft rate (Ω) relative to the impeller at the flow $\phi=0.09$. It is also found that this rotational speed varies depending on the flow rate.

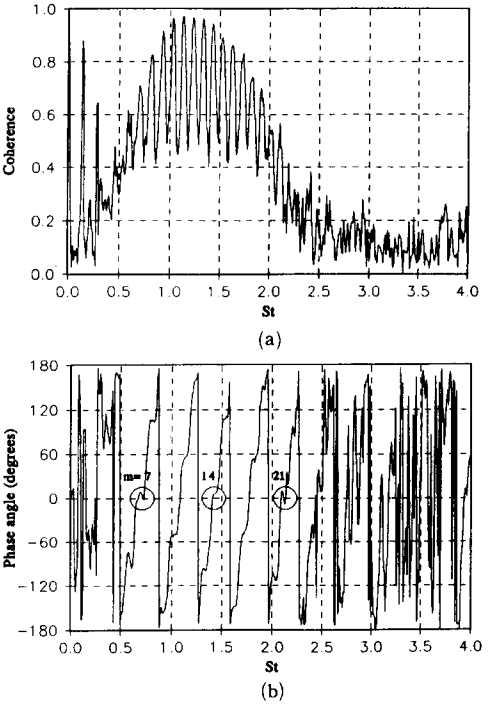

Fig. 13 (a) Coherence and
(b) Phase angle of cross-spectra between pressures at 1 & 3

Another important thing to notice from Fig. 13(b) is that the curve crosses the line of zero angle at the frequencies corresponding to the mode numbers which are multiples of impeller blade number, i.e., $m=7$, 14, and 21. These points are marked with circles on the figure. There are several additional frequency locations that the curve crosses the zero angle line, however they are not related to any integer mode numbers. This is an important result that will help to understand the noise generation mechanism. Further discussion will be presented later in this paper.

3.5 Propagation of the unsteady flow pattern

In order to investigate how the flow instability found in the impeller passage propagates to the downstream a single hot-wire sensor is placed near the discharge of the impeller. The axial location of the probe was fixed to be the center of the blade passage. The data measured at $\Delta r/R=0.02$ clearly show the blade passage frequency (BPF) peak at $St=1.0$ (Fig. 14). This is due to the non-uniform flow distribution from passage to passage revealed in the phase averaged velocity data. In addition, a set of broadened peaks are present at lower and higher frequencies. These lower frequency peaks are harmonically related, with a Strouhal number difference of about 0.043. The largest amplitude peak in the cluster is at a Strouhal number of 0.44. The cluster of peaks at higher frequency around the Strouhal number 1.4 are believed to be generated by the modulation of

the lower frequency peaks and the blade passage tone.

It is interesting to find that the Strouhal numbers at which the peaks occur in the flow velocity spectrum in stationary coordinates (Fig. 14) are different from those in the flow velocity spectrum referenced to rotating coordinates (Fig. 10(d)). These two sets of data were both taken at the same flow condition ($\phi=0.09$). The spectrum from the rotating hot-wire shows peaks at Strouhal numbers which are clustered about a Strouhal number of 1.2. The Strouhal number differences between the peaks are related to 0.7 impeller rps (or $St\approx0.1$). There is no peak at a Strouhal number of one, the blade passage frequency. This is due to the absence of spatial non-uniformity relative to the rotating hot-wire. Moreover, the cluster of peaks near $St=1.2$ in Fig. 10(d) moved to the lower frequency near $St=0.4$ in Fig. 14. The shifting in the frequency locations is due to the different rotating speed of the pattern in each measurement frames.

The rotational speed of this pattern can be estimated from two stationary hot-wires at the discharge. The estimated angular speed was found to be 28% of the shaft speed in the same rotational direction as the impeller for all the modes. It is interesting to compare the rotational speed of the pattern in the stationary frame (ω_S) with the one measured in the rotating frame (ω_R). As was estimated from two pressure sensor correlation, the ω_R was 72% of the shaft speed, opposite to the impeller rotation direction. Therefore, the origin of the cluster of peaks at the lower frequency in Fig. 14 is the same as the ones found in Fig. 10(d), although their frequencies are different. The amount of frequency shift is directly related to the rotational speed of the pattern. For example, the Strouhal number of mode 11 in the rotating frame moved from 1.13 to 0.44 in the stationary frame. This is proportional to the angular speed ratio $28/72=0.39$. Similarly, the spacing between the peaks changed with the same ratio.

3.6 Relationship between the unsteady flowfield and the radiated noise

As discussed above, the rotating flow instability at the discharge of the impeller is coupled to the unsteady flow fluctuations in the impeller blade passages. By interacting with the impeller blades, the destabilized passage flow induces unsteady pressure on the blade surface, most dominantly near the trailing edges. In Fig. 15(a) the radiated noise spectrum measured with a microphone in the acoustic far field is compared with the spectrum of the surface pressure on an impeller blade (pressure sensor 1) for the flow

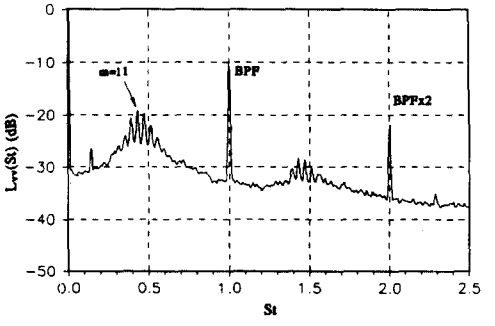

Fig. 14 Spectra of the discharge velocity at $\Delta r/R=0.02$

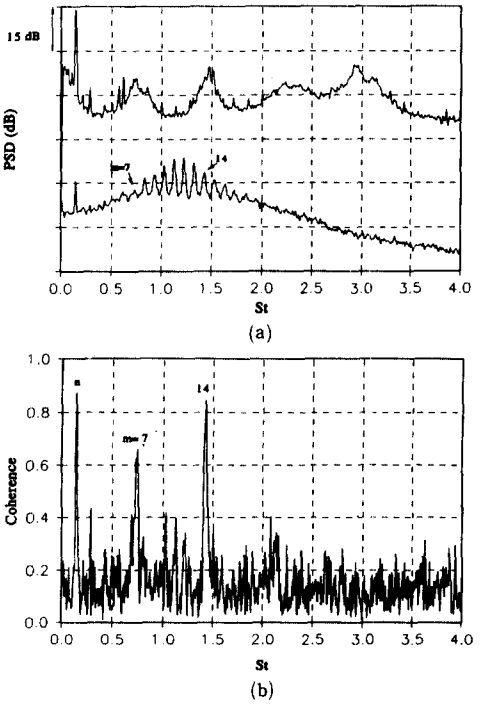

Fig. 15 (a) Far-field noise, surface pressure and (b) Their coherence

rate of $\phi=0.09$. The location of the microphone was 2.44 meters (8 feet) from the center of the impeller in the same plane as the rotation of the impeller. In the noise spectrum, broad humps appear which are centered at $St\approx0.7$ and $St\approx1.4$ and correspond to the first two peaks in the source strength spectral distribution function (F function) in Fig. 6. The higher harmonic humps observed in Fig. 6 are not noticeable from the far-field noise spectrum in Fig. 15(a) because they are buried in the background noise generated from the driving system. This again illustrates the value of the spectral decomposition procedure.

Comparing the noise and the surface pressure spectrum in Fig. 15(a), it can be seen that the low amplitude peaks at $m=7$ and $m=14$ in the surface pressure spectrum generate more acoustic noise than the modes with higher amplitudes ($m=8,9\cdots13$). This is due to a possible near field pressure cancellation described below. All the modes in the pressure spectrum will generate noise from each blade, but the modes synchronized with the number of impeller blades ($m=7$, $14,21\cdots$) generate noise most efficiently. This can be verified from the phase of the cross-spectrum between surface pressures on two separate blades shown in Fig. 13(b). Only the spectral peaks that correspond to multiples of the number of impeller blades are in-phase. All other peaks in the surface pressure cross-spectra are out-of-phase. For example, all seven lobes in the pattern with $m=7$ induce unsteady pressure on the seven impeller blades simultaneously, or in-phase, while the instability pattern is rotating around the impeller. In contrast to this, the number of lobes in the pattern with $m=8$ do not match with the number of impeller blades. So, it appears that acoustic waves from different blades interfere with each other and result in relatively little noise propagating to the far-field at the frequency.

The coherence between the noise and the surface pressure, shown in Fig. 15(b), demonstrates the high correlation level at the frequencies corresponding to $m=7$ and $m=14$. The peak at $St\approx0.14$, i.e. shaft rate, in the noise and coherence spectra is generated from the slip-ring unit mounted on the motor shaft. High coherence level at $m=7$ and $m=14$ indicate that the peaks in the noise spectrum are generated from the unsteady pressure fluctuation on the impeller blades. Strictly speaking, a high coherence level between signals from two sensors does not necessarily mean a direct correlation between them; a signal generated from a third source can also produce a high coherence level between those two sensors. However, an experiment performed by Mongeau(1991) has shown that a small change in trailing edge shape dramatically affected the generated noise spectra, which further suggests a strong correlation between impeller surface pressure and the radiated noise.

4. Discussion

After considering all the evidence, it is proposed here that the jet-wake flow structure at the discharge causes the jet side of the flow to convect from one passage to the exit of the adjacent passage and disturb the flow in that passage. Therefore, the onset of the disturbance and its magnitude are closely related to the blade loading near the discharge, because the pressure difference across the trailing edge is the one causing the flow to move. The blade discharge angle is also an important factor because the ratio of the radial to tangential velocity components is directly controlled by the discharge geometry.

Flow migration from one passage to another was also noticed by Fowler(1968). In an isolated rotating channel, the flow at the exit showed a stable and uniform velocity profile. When the channel was exposed to neighboring channels, however, a drastic change in flow distribution was observed. The channel flow became very similar to that seen in a complete impeller, and showed an unstable jet-wake pattern at the discharge. The low radial outflow in the wake allowed backflow into this region, and this consequently destabilized the jet-wake flow in the passage. These phenomena were also observed by Dean(1970), and were postulated to be a source of noise generation and resonance phenomena acting on the impeller and diffuser channels. However, to the author's knowledge, no detailed anal-

ysis of the relationship between this type of flow and radiated noise has been previously reported.

As stated earlier, the unsteady flow phenomenon at the discharge is very similar in its behavior to rotating stall in a centrifugal impeller or diffuser. The origin and some of the characteristics are, however, quite different from either type of rotating stall. Rotating stall is a form of flow instability appearing during operation of compressors in reduced flow rates. In impeller stall, the unsteadiness begins early in the impeller passages, usually at the leading edge of blades. The flow instability in the upstream triggers flow separation in one or more passages and results in less flow rate through the passages. Lennemann and Howard(1970) observed a boundary layer separation in the impeller passage which is strongly influenced by the secondary flow. The cause of the instability that triggers the flow separation is not yet known, but the behavior of the phenomenon is relatively well understood. When a stall occurs the axisymmetry of the impeller or discharge flow no longer exists. The shape of this discharge non-uniformity depends on the number of stalled regions (or stall cells) and their relative strength. The number of modes of the discharge pattern found in most axial or centrifugal compressors is less than the number of impeller blades. The rotating stall in a vaneless diffuser is caused by a flow instability of the inviscid core flow which exists in the radial diffuser (see Abdelhamid, 1979 and Abdelhamid & Bertrand, 1979). It is also found that a flow separation occurs in the radial diffuser when the diffuser stalls (Jansen, 1964). Jansen proposed that negative radial flow in the impeller discharge induces the rotating stall in the diffuser.

Unlike the rotating stall in an impeller or diffuser, the discharge flow instability characterized in the present study was found to be occurring most predominantly at medium flow rates. It was also found that the number of modes of the instability is larger than the number of impeller blades, which is quite unusual in impeller rotating stall. As the unsteady flow measurement in the impeller passages has proved, the discharge instability started only at the exit of the impeller and showed no indication of stall in the passages. In addition, the discharge instability is also different from the diffuser stall phenomenon, since there is no diffuser channel to cause flow separation in the present configuration. As a conclusion, the discharge flow instability found in this study can not be characterized as either an impeller or a diffuser rotating stall. It is however suspected to be a cause of the diffuser rotating stall by interacting with the boundary layer on the diffuser wall. When a diffuser stalls, the rotating speed and the shape of the instability pattern is strongly affected by the separated region in the diffuser passage. Uncovering the proposed transition mechanism would be useful in understanding the origin of the diffuser rotating stall in a centrifugal machine.

5. Conclusions

(1) In this research, an experimental investigation on the unsteady flowfield and noise generation mechanism of a centrifugal turbomachine has been performed successfully. The radiated noise spectra were shown to be dominated by harmonically related broad humps. These were proven to be generated by the interaction of a coherent unsteady flow structure rotating around the impeller discharge and the trailing edges of the impeller blades.

(2) The jet-wake flow pattern found in the impeller blade passages induces a strong vorticity field near the trailing edge of each blade. This unstable vorticity flow motion influences the flow discharging from the adjacent passage, and destabilizes the jet-wake flow in the passage.

(3) The unstable passage flow causes a periodic pressure fluctuation on the blade surfaces. This unsteady flow is found to be coherent from blade to blade and forms a rotating instability pattern around the impeller discharge. This instability pattern has a rich harmonic content and a well defined precessing speed.

(4) The rotating discharge instability in the impeller discharge is very similar in its behavior to the phenomenon known as rotating stall found in centrifugal impellers and diffusers. The origin of each of these flows and some of their characters

are found to be quite different.

(5) The surface pressure spectrum measured at the trailing edge of each blade revealed a cluster of peaks which were identified with integer mode numbers. The modes synchronized with the number of impeller blades (mode 7, 14, 21,...) were shown to generate noise more efficiently than the other modes.

References

Abdelhamid, A. N., 1980, "Analysis of Rotating Stall in Vaneless Diffusers of Centrifugal Compressors," ASME Paper No. 80-GT-184.

Abdelhamid, A. N. and Bertrand, J., 1979, "Distinctions Between Two Types of Self Excited Gas Oscillations in Vaneless Radial Diffusers," ASME Paper No. 79-GT-58.

Bent, P. H., 1993, *The Influence of the Discharge Configuration on the Generation of Broadband Noise in Centrifugal Turbomachinery,* Ph. D. Thesis, The Pennsylvania State University, University Park.

Cho' '.-S., 1991, *Experiments on the Unsteady Flowfield Associated with Noise Generation in Centrifugal Turbomachinery,* Ph. D. Thesis, The Pennsylvania State University, University Park.

Dean, Jr., R. C. and Senoo, Y., 1960, "Rotating Wakes in Vaneless Diffusers," ASME Journal of Basic Engineering, pp. 563~570.

Dean, Jr., R. C., 1970, "Boundary Layers in Centrifugal Compressors," Fluid Mechanics, Acoustics and Design of Turbomachinery, A symposium held at The Pennsylvania State University, University Park, August 31-Spetember 3.

Eckardt, D., 1975, "Instantaneous Measurements in the Jet-Wake Discharge Flow of a Centrifugal Compressor Impeller," ASME Journal of Engineering for Gas Turbine and Power, Vol. 97, pp. 337~346.

Embleton, T. F. W., 1963, "Experimental Study of Noise Reduction in Centrifugal Blowers," Journal of the Acoustical Society of America, Vol. 35, pp. 700~705.

Fowler, H. S., 1968, "The Distribution and Stability of Flow in a Rotating Channel," ASME Journal of Engineering for Gas Turbine and Power, Vol. 90, No. 3, pp. 229~236.

Gilman, F. C., 1968, "Testing Pumps as Fan and Fans as Pumps," ASME Journal of Engineering for Gas Turbine and Power, Vol. 90, pp. 140~143.

Gostelow, J. P., 1984, *Cascade Aerodynamics,* Pergamon Press.

Hah, C. and Lakshminarayana, B., 1978, "Effect of Rotation on a Rotating Hot-wire Sensor," Journal of Physics E : Instrum., Vol. 11.

Jansen, W., 1964, "Rotating Stall in a Radial Vaneless Diffuser," ASME Journal of Basic Engineering, Vol.86, No. 4, pp. 750~758.

King, J. A., 1968, "Testing Pumps in Air," ASME Journal of Engineering for Gas Turbine Power, pp. 97 ~105.

Lennemann, E. and Howard, J. H. G., 1970, "Unsteady Flow Phenomena in Rotating Centrifugal Impeller Passages," ASME Journal of Engineering for Power, Gas Turbine and Power, Vol. 92, No. 1, pp. 65 ~72.

Mongeau, L. G., 1991, *Experimental Study of the Mechanism of Sound Generation by Rotating Stall in Centrifugal Turbomachines,* Ph.D. Thesis, The Pennsylvania State University.

Neise, W., 1976, "Noise Reduction in Centrifugal Fans: a literature survey," Journal of Sound and Vibration, Vol. 45, No. 3, pp. 375~403.

Neise, W. and Barsikow, B., 1982, "Acoustic Similarity Laws for Fans," ASME Journal of Engineering for Industry, Vol. 104, pp. 162~168.

Tourret, J., Badie-Cassagnet, A., Bernard, G., Foucault, J. P. and Kermarec, J., 1985, "Experimental Studies of Noise Emission and Noise Generation from a Centrifugal Pump," ASME paper No. 95-WA/FE-8.

Westphal, R. V. and Mehta, R. D., 1984, "Crossed Hot-Wire Data Acquisition and Reduction System," NASA TM-85871.